IOP Publishing New J. Phys. 27 (2025) 074102 https://doi.org/10.1088/1367-2630/ade7a9

New Journal of Physics
The open access journal at the forefront of physics

Deutsche Physikalische Gesellschaft DPG
IOP Institute of Physics

Published in partnership with: Deutsche Physikalische Gesellschaft and the Institute of Physics

OPEN ACCESS

RECEIVED
17 February 2025

REVISED
8 June 2025

ACCEPTED FOR PUBLICATION
24 June 2025

PUBLISHED
3 July 2025

PAPER

Heralded fidelity-robust high-dimensional quantum computing

Fang-Fang Du[1], **Zhi-Guo Fan**[1,*], **Zhuo-Ya Bai**[2] and **Qiu-Lin Tan**[1,*]

[1] Key Laboratory of Micro/nano Devices and Systems, Ministry of Education, North University of China, Tai Yuan 030051, People's Republic of China
[2] Beijing National Research Center for Information Science and Technology, Department of Electronic Engineering, Tsinghua University, Beijing 100084, People's Republic of China
* Authors to whom any correspondence should be addressed.

E-mail: zhiguo_fan2023@163.com and tanqiulin@nuc.edu.cn

Keywords: quantum computing, quantum gate, high dimension, quantum information technology

Abstract

In high-dimensional quantum systems, qudits offer a richer resource than traditional two-dimensional qubits, increasing the capacity of quantum channels and enhancing the efficiency of fault-tolerant quantum computation. These advantages can be utilized to solve complex problems across various fields. In the paper, we propose a 2-qudit controlled-NOT (CNOT) gate in a 4×4-dimensional space and a 3-qudit controlled-controlled-NOT (Toffoli) gate in a $4 \times 4 \times 4$-dimensional space, both equipped with error-heralded units. Our designs do not require auxiliary photons or extra negatively charged nitrogen-vacancy (NV^-) center, resulting in saving resources. Moreover, since the imperfect NV^--cavity interaction processes are predicted in real-time by sensitive single-photon detectors, both high-dimensional CNOT and Toffoli gates boast robust fidelities using existing technology. Furthermore, our protocols simplify circuits with error-heralded units, significantly contributing to the effectiveness of quantum information technology and paving the way for advanced high-dimensional quantum computing.

1. Introduction

Quantum computing offers substantial advantages over classical computing, enabling solutions to previously intractable problems across various fields [1]. Quantum logic gates are at the core of many quantum computing tasks [2–6]. Traditional two-dimensional quantum gates, such as one-qubit X gate, two-qubit controlled-NOT (CNOT) gate, and three-qubit controlled-controlled-NOT (Toffoli) gate, perform logic operations on a qubit system (represented by $|0\rangle$ and $|1\rangle$) [7–9]. These gates allow for the construction of arbitrary quantum operations and serve as benchmarks for universal quantum computation [10, 11]. However, these gates face limitations in large-scale quantum computing due to fidelity issues and resource constraints. Beyond two-dimensional qubits, qudit systems with d (where $d > 2$) dimension have emerged as valuable resources, extending the capacity to encode and process information more efficiently in high-dimensional quantum systems [12–15]. The larger Hilbert space offered by qudits presents several advantages over qubits. This expanded space simplifies the construction of quantum gates [16–18], improves the efficiency of fault-tolerant quantum computation [19, 20], increases quantum channel capacity [21, 22], and enhances communication security [23–25]. Additionally, qudits enable stronger violations of Bell-type inequalities [26–28] and exhibit greater resilience to noise [29–31]. Qudit-based quantum information technology (QIT) has been both theoretically explored and experimentally implemented across various physical systems [32–41].

The CNOT and Toffoli gates have wide-ranging applications, including quantum algorithms [42], quantum error correction [43], quantum arithmetic operations [44], and fault-tolerant quantum computing [45]. Numerous theoretical approaches have been developed to realize these gates in various physical systems [46–58]. Experimentally, the CNOT and Toffoli gates have been implemented in nuclear magnetic resonance [59], linear optics [60], trapped ions [61], circuit quantum electrodynamics [62], neutral atoms [63], and silicon spin qubits [64]. In 2024, Nie *et al* examined the exact implementation of the n-Toffoli gate and the

n-controlled U gate using quantum circuits composed solely of single-qubit gates and CNOT gates [65]. These linear and nonlinear quantum gates are encoded using binary variables [66]. The standard 2×2-dimensional CNOT gate and $2 \times 2 \times 2$-dimensional Toffoli gate are expressed as $U^2_{\mathrm{CNOT}}|x,y\rangle = |x,(x+y)\%2\rangle$ and $U^2_{\mathrm{Toffoli}}|x,y,z\rangle = |x,y,(z+xy)\%2\rangle$, respectively, where $x,y,z \in \{0,1\}$, and % denotes the modulo operation [67–69]. As circuit complexity grows, the limitations of traditional two-dimensional gates become more apparent, driving the need for more advanced gate designs. In 2023, Zi *et al* presented a linear-size synthesis scheme for Toffoli gate on d-dimensional ($d > 2$) qudits using just one ancilla [70]. Specifically, the d-dimensional CNOT and Toffoli gate can be expressed as $U^d_{\mathrm{CNOT}}|x,y\rangle = |x,(x+y)\%d\rangle$ and $U^d_{\mathrm{Toffoli}}|x,y,z\rangle = |x,y,(z+xy)\%d\rangle$, where $x,y,z \in \{0,1,\ldots,d-1\}$. Gao *et al* put forward $2 \times 2 \times 4$-dimensional Toffoli gate in orbital angular momentum degrees of freedom of a single photon assisted by entangled states with the low efficiency 1/172 [71]. Operating in a larger Hilbert space, high-dimensional CNOT and Toffoli gates can process more information through parallel quantum channels. The increased dimensionality not only enables more complex computations but also enhances processing power, underscoring the need to further explore the construction of high-dimensional CNOT and Toffoli gates with improved fidelity and efficiency.

Hybrid quantum gates, involving various types of qubits, have garnered significant attention [72–75]. These hybrid gates facilitate the transfer of quantum states between quantum processors and memories, as well as the generation of entangled states between memory and processor units [76, 77]. A key component in the construction of hybrid quantum gates is the electron spin of the negatively charged nitrogen-vacancy (NV^-) center, which supports optical initialization and enables fast single-qubit operations [78–81]. Moreover, the electron spins of NV^- centers can maintain millisecond-scale coherence times, ensuring the successful operation of quantum gates [82]. NV^- centers have proven to be highly effective in applications [83–85]. To date, single-qubit, universal multi-qubit, and CNOT gates have been successfully implemented on the electron spin platform of NV^- centers [86–89]. Building on this foundation, we aim to utilize the hybrid photon-NV^- center system to establish high-dimensional CNOT and Toffoli gates.

In this paper, we present two novel approaches to realizing deterministic hybrid CNOT and Toffoli gates in 4×4 and $4 \times 4 \times 4$ dimensions, respectively, using error-heralded quantum units without the need for auxiliary qubits. In our high-dimensional CNOT gate scheme, the electron-spin states of two NV^- centers and the polarization-spatial states of a single photon are used to encode the target and control qudits, respectively. Crucially, detectors of three error-predicted units allow for the immediate detection of errors caused by imperfect interactions between photons and NV^- centers.

The paper is organized as follows. An NV^- center is introduced briefly in section 2. In section 3, error-predicted units, i.e. I_i, M_i, N_i, are presented. In section 4, the 4×4-dimensional CNOT gate is presented and the $4 \times 4 \times 4$-dimensional Toffoli gate is introduced in section 5. We provide a brief discussion and a summary in section 6.

2. An NV^- center

To advance quantum information, establishing a link between individual spins and single photons is essential. This is achieved through the use of an NV^- center, as shown in figure 1(a), positioned within a single-sided optical cavity. The system consists of four components, including a substituted nitrogen atom, electrons contributed by two types of atoms, and a vacancy. The cavity features a bottom mirror that is fully reflective and a top mirror that is partially reflective. The energy levels of the NV^- center are intricate, shaped by the complex interaction of electron-nuclear coupling and optical transitions. In the ground state, spin–spin interactions cause a splitting into $|0\rangle$ (with $m_s = 0$) and $|\pm\rangle$ (with $m_s = \pm 1$), separated by a 2.87 GHz zero-field splitting. One of the excited states, $|A_2\rangle = (|E_-\rangle|+\rangle + |E_+\rangle|-\rangle)/\sqrt{2}$, captures both spin–orbit and spin–spin effects, exhibiting symmetric properties that ensure stability. The orbital states $|E_\pm\rangle|(J_s = \pm 1)$ represent the coupling dynamics between the resonator and the NV^- center system. The optical transition between the spin states $|+\rangle \leftrightarrow |A_2\rangle$ (or $|-\rangle \leftrightarrow |A_2\rangle$) is facilitated by the absorption or emission of left- (right-) circularly polarized photons, $|R\rangle$ ($|L\rangle$). The efficiency of this process is enhanced when the NV^- center is embedded in a frequency-degenerate two-mode cavity. The Hamiltonian for the cavity-NV^--center system, within the rotating wave approximation, is expressed as

$$\begin{aligned}\hat{H} = {} & \hbar\omega_s|A_2\rangle\langle A_2| + \hbar\omega_{c,L}\hat{a}^\dagger_L\hat{a}_L + \hbar\omega_{c,R}\hat{a}^\dagger_R\hat{a}_R \\ & + \hbar g\left(\hat{a}_L\hat{\sigma}_+ + \hat{a}^\dagger_L\hat{\sigma}_- + \hat{a}_R\hat{\sigma}^\dagger_+ + \hat{a}^\dagger_R\hat{\sigma}_+\right), \end{aligned} \tag{1}$$

here ω_s, $\omega_{c,L}$, and $\omega_{c,R}$ represent the photon and cavity frequencies linked to the NV^- center, while $\hat{\sigma}_+(\hat{\sigma}^\dagger_+)$ and $\hat{\sigma}_-(\hat{\sigma}^\dagger_-)$ correspond to the raising and lowering of energy levels in the NV^- center, respectively. The

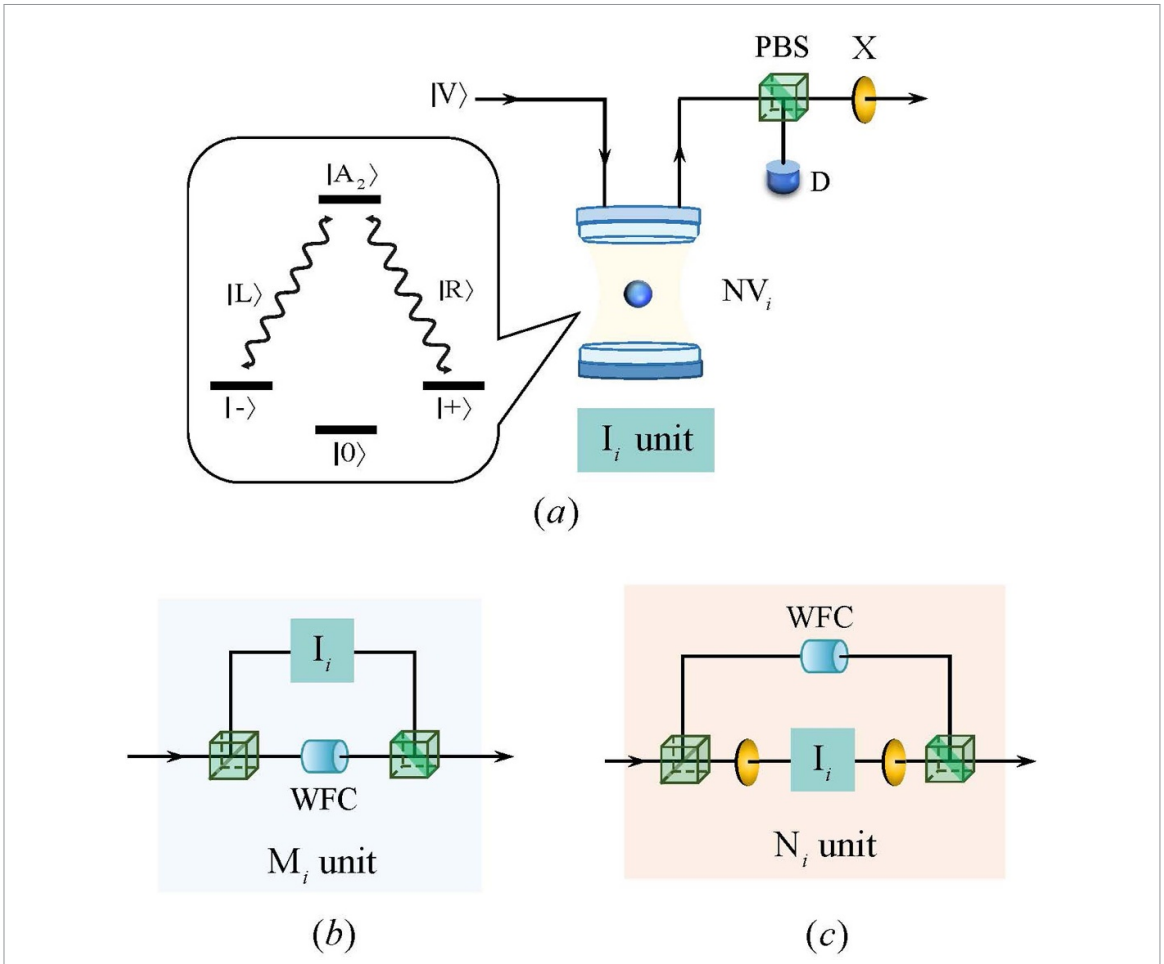

Figure 1. Schematic diagrams of the error-predicted (a) I_i unit, (b) M_i unit and (c) N_i unit. PBS represents a polarization beam splitter, which transmits the horizontal-polarized photon $|H\rangle$ and reflects a vertical-polarized photon $|V\rangle$. X is a half-wave plate, which performs bit-flip operation on the photon $\sigma_x^{\mathrm{p}} = |H\rangle\langle V| + |V\rangle\langle H|$. D is a single-photon detector. WFC is a wave-form corrector that executes the coefficient variation $|H\rangle\ (|V\rangle) \rightarrow r_-(\Delta)|H\rangle(|V\rangle)$.

operators $\hat{a}_R$ and $\hat{a}_L$ (along with their adjoints, $\hat{a}_{\mathrm{R}}^{\dagger}$ and $\hat{a}_{\mathrm{L}}^{\dagger}$) act as annihilation (creation) operators for the cavity field. Additionally, g is the coupling strength between the single-sided cavity and the NV^- center.

When the input photon couples with NV^--cavity system, the Heisenberg equations of the system and input and output relation of field operators are [90]

$$\begin{aligned}
\frac{\mathrm{d}\hat{a}}{\mathrm{d}t} &= -\left[i(\omega_{\mathrm{c}}-\omega)+\frac{\kappa+\kappa_{\mathrm{s}}}{2}\right]\hat{a} - g\hat{\sigma} - \sqrt{\kappa}\hat{a}_{\mathrm{in}} - \sqrt{\kappa_{\mathrm{s}}}\hat{s}_{\mathrm{in}},\\
\frac{\mathrm{d}\hat{\sigma}}{\mathrm{d}t} &= -\left[i(\omega_{\mathrm{s}}-\omega)+\frac{\gamma}{2}\right]\hat{\sigma} - g\hat{\sigma}_z\hat{a} + \sqrt{\gamma}\hat{\sigma}_z\hat{N},\\
\hat{a}_{\mathrm{out}} &= \hat{a}_{\mathrm{in}} + \sqrt{\kappa}\hat{a}.
\end{aligned} \tag{2}$$

The noise operator is $\hat{N}$, while $\hat{a}_{\mathrm{in}}$, $\hat{a}_{\mathrm{out}}$, and $\hat{s}_{\mathrm{in}}$ represent the input, output, and side-leakage field operators, respectively. γ is the decay rate of the NV^- center population. Furthermore, the population inversion operator for the system is given by $\hat{\sigma}_z = \hat{\sigma}_+\hat{\sigma}_- - \hat{\sigma}_-\hat{\sigma}_+$. Under weak excitation conditions, where $\langle\hat{\sigma}_z\rangle = -1$, the reflection coefficient $r(\omega, g)$ for a photon interacting with the unidirectional cavity-NV^- system is determined as

$$r(\omega,g) = \frac{\left[i(\omega_{\mathrm{s}}-\omega)+\frac{\gamma}{2}\right]\left[i(\omega_{\mathrm{c}}-\omega)-\frac{\kappa}{2}+\frac{\kappa_{\mathrm{s}}}{2}\right]+g^2}{\left[i(\omega_{\mathrm{s}}-\omega)+\frac{\gamma}{2}\right]\left[i(\omega_{\mathrm{c}}-\omega)+\frac{\kappa}{2}+\frac{\kappa_{\mathrm{s}}}{2}\right]+g^2}. \tag{3}$$

When $\omega_{\mathrm{c}} = \omega_{\mathrm{s}}$, the reflection coefficient is simplified to

$$r(\Delta,g) = \frac{\left(i\Delta+\frac{\gamma}{2}\right)\left(i\Delta-\frac{\kappa}{2}+\frac{\kappa_{\mathrm{s}}}{2}\right)+g^2}{\left(i\Delta+\frac{\gamma}{2}\right)\left(i\Delta+\frac{\kappa}{2}+\frac{\kappa_{\mathrm{s}}}{2}\right)+g^2}. \tag{4}$$

Here, $\Delta = \omega_c - \omega = \omega_s - \omega$ represents the detuning between the incident photon and the cavity mode. Assuming g is zero, indicating no coupling between the photon and the NV$^-$ center, the uncoupled reflection coefficient $r(\Delta,0)$ is expressed as

$$r(\Delta,0) = \frac{i\Delta - \frac{\kappa}{2} + \frac{\kappa_s}{2}}{i\Delta + \frac{\kappa}{2} + \frac{\kappa_s}{2}}. \tag{5}$$

Due to the spin-selection rule and cavity quantum electrodynamics effects, $r(\Delta,g)$ represents the reflection coefficient in the coupled state, while $r(\Delta,0)$ represents the reflection coefficient in the uncoupled state. Considering that the photon in $|L\rangle$-polarized state interacts with the NV$^-$-cavity system, wherein the NV$^-$ spin is initially in the state $|\psi\rangle = \alpha|+\rangle + \beta|-\rangle$, with the sum of the squares of the coefficients, $|\alpha|^2 + |\beta|^2$, equaling 1. The state of the photon-spin system evolves into $|\psi'\rangle = |L\rangle[r(\Delta,g)\alpha|+\rangle + r(\Delta,0)\beta|-\rangle]/\sqrt{p_0}$. Here, $p_0 = |r(\Delta,g)\alpha|^2 + |r(\Delta,0)\beta|^2$ quantifies the probability that the photon is reflected by the NV$^-$-cavity system. When a vertically polarized photon, i.e. $|V\rangle = -i(|R\rangle - |L\rangle)/\sqrt{2}$, interacts the NV$^-$-cavity system with the NV$^-$ spin initially set in the state $|1\rangle = (|+\rangle + |-\rangle)/\sqrt{2}$ or $|0\rangle = (|+\rangle - |-\rangle)/\sqrt{2}$, the resulting entangled state of the whole system adheres to the following principles

$$\begin{aligned} |V\rangle|1\rangle &\rightarrow [ir_+(\Delta)|V\rangle|1\rangle + r_-(\Delta)|H\rangle|0\rangle]/\sqrt{p_1}, \\ |V\rangle|0\rangle &\rightarrow [ir_+(\Delta)|V\rangle|0\rangle + r_-(\Delta)|H\rangle|1\rangle]/\sqrt{p_1}. \end{aligned} \tag{6}$$

Here, $|H\rangle = (|R\rangle + |L\rangle)/\sqrt{2}$, $r_\pm(\Delta) = [r(\Delta,0) \pm r(\Delta,g)]/2$, and $p_1 = [|r(\Delta,0)|^2 + |r(\Delta,g)|^2]/2$ represents the probability that the photon interferes in the reflection geometry.

3. Error-heralded units

3.1. I_i unit

Based on the interaction rules in equation (6) between single photon and the spin of NV$^-$ centers mentioned earlier, now the I_i unit is introduced, where the subscript i represents the electron spin of ith NV$^-$ center. Assuming the initial state of the NV_i^- center is $|+\rangle_i$ ($|-\rangle_i$), and the photon is set to the $|V\rangle$-polarized state, the process depicted on the right of figure 1(a) unfolds. In the circuit, the polarizing beam splitter (PBS) transmits (reflects) $|H\rangle(|V\rangle)$-polarized photons, and the half-wave plate (X) fixed at $\theta = 45°$ facilitates the interconversion, i.e. $|H\rangle \leftrightarrow |V\rangle$. Once the photon enters the circuit, it interacts with the spin of the NV_i^- center. Consequently, the hybrid state of the electron spin and the photon is evolved into superposition states

$$\begin{aligned} |V\rangle|+\rangle_i &\rightarrow ir_+(\Delta)|V\rangle|+\rangle_i + r_-(\Delta)|H\rangle|+\rangle_i, \\ |V\rangle|-\rangle_i &\rightarrow ir_+(\Delta)|V\rangle|-\rangle_i - r_-(\Delta)|H\rangle|-\rangle_i. \end{aligned} \tag{7}$$

As shown in equation (7), ignoring the electron spin states, the photon generates two different polarization state outputs. Specifically, the $|V\rangle$-polarized state is reflected by the PBS and then detected by detector D, indicating an error occurrence with an efficiency of $|r_+(\Delta)|^2$. In this case, both the polarization state and the electron spin stay the same. On the other hand, if detector D does not react, this indicates the successful transmission of the $|H\rangle$-polarized photon through the PBS with an efficiency of $|r_-(\Delta)|^2$. This principle underpins the operation of the error-heralded unit. Ultimately, the $|H\rangle$-polarized photon, after passing through the X, undergoes a bit-flip operation, i.e. $|H\rangle \leftrightarrow |V\rangle$. When the detector D is not triggered, the hybrid state of the system in the transmission path evolves into

$$\begin{aligned} |V\rangle|+\rangle_i &\rightarrow r_-(\Delta)|V\rangle|+\rangle_i, \\ |V\rangle|-\rangle_i &\rightarrow -r_-(\Delta)|V\rangle|-\rangle_i. \end{aligned} \tag{8}$$

Apparently, after the PBS passively filters out the erroneous entangled state, the value of $|r_-(\Delta)|$ may vary with different factors, such as the frequency detuning Δ/κ, the cavity decay rate κ_s/κ, and the coupling rate g/κ. However, it primarily affects the efficiency of the photon-spin interaction as a global coefficient.

3.2. M_i unit

The M_i and N_i units, which incorporate the I_i unit, possess the same error-heralded functionality. Furthermore, the design of the M_i and N_i units can effectively simplify the circuits for high-dimensional

quantum gates. Therefore, it is essential to elaborate on the design of their quantum circuits and their specific functions.

For the M_i unit illustrated in figure 1(b), consider that the initial spin state of the NV_i^--cavity system is $|+\rangle$ ($|-\rangle$), and the photon is set to the $|H\rangle$- ($|V\rangle$-)polarized state. After the photon passes through left-side PBS, its $|H\rangle$-polarization state undergoes the wave-form corrector (WFC), which executes the coefficient variation from $|H\rangle(|V\rangle)$ to $r_-(\Delta)|H\rangle(|V\rangle)$, and the $|V\rangle$-polarization state undergoes I_i unit, then they converge on right-side PBS. If the detector D of the I_i unit remains inactive, the hybrid state of photon and the NV_i^- center undergoes evolution into

$$\begin{aligned}
&|H\rangle|+\rangle_i \to r_-(\Delta)|H\rangle|+\rangle_i,\\
&|H\rangle|-\rangle_i \to r_-(\Delta)|H\rangle|-\rangle_i,\\
&|V\rangle|+\rangle_i \to r_-(\Delta)|V\rangle|+\rangle_i,\\
&|V\rangle|-\rangle_i \to -r_-(\Delta)|V\rangle|-\rangle_i.
\end{aligned} \tag{9}$$

If before and after the input photon interacts with the M_i unit, it undergoes Hadamard operations H^p with the half-wave plate (H) fixed at $\theta = 22.5°$, facilitating the transformation, i.e. $|H\rangle \xrightarrow{H^p} (|H\rangle + |V\rangle)/\sqrt{2}$ and $|V\rangle \xrightarrow{H^p} (|H\rangle - |V\rangle)/\sqrt{2}$, the modification ($H^p \to$ interaction with M_i unit$\to H^p$) results in the hybrid state of the system without D triggered evolving into

$$\begin{aligned}
&|H\rangle|+\rangle_i \to r_-(\Delta)|H\rangle|+\rangle_i,\\
&|H\rangle|-\rangle_i \to r_-(\Delta)|V\rangle|-\rangle_i,\\
&|V\rangle|+\rangle_i \to r_-(\Delta)|V\rangle|+\rangle_i,\\
&|V\rangle|-\rangle_i \to r_-(\Delta)|H\rangle|-\rangle_i.
\end{aligned} \tag{10}$$

According to equation (10), if the spin state is $|-\rangle_i$, the polarization state of the photon is flipped; otherwise, it remains unchanged. This condition serves as the prerequisite for the accurate classification of control qudits of high-dimensional quantum gates.

Similarly, if before and after the input photon interacts with the M_i unit, the electron spin of the NV_i^- center of the M_i unit executes Hadamard operation H_i^e via a $\pi/2$ microwave pulse [91], i.e. $|+\rangle \xrightarrow{H_i^e} 1/\sqrt{2}(|+\rangle + |-\rangle)_i$ and $|-\rangle \xrightarrow{H_i^e} 1/\sqrt{2}(|+\rangle - |-\rangle)_i$, this modification ($H_i^e \to$ interaction with M_i unit$\to H_i^e$) results in the hybrid state of the system without D triggered evolving into

$$\begin{aligned}
&|H\rangle|+\rangle_i \to r_-(\Delta)|H\rangle|+\rangle_i,\\
&|H\rangle|-\rangle_i \to r_-(\Delta)|H\rangle|-\rangle_i,\\
&|V\rangle|+\rangle_i \to r_-(\Delta)|V\rangle|-\rangle_i,\\
&|V\rangle|-\rangle_i \to r_-(\Delta)|V\rangle|+\rangle_i.
\end{aligned} \tag{11}$$

According to equation (11), if and only if the polarization state is $|V\rangle$, the spin state of the NV_i^- center is flipped. The rules serve as the precise operation of target qudits of 4-dimensional quantum gates.

In a word, the M_i unit combining with two types of Hadamard operations H^p on the photon and H^e on the electron spin of the NV_i^- center, performs two key functions: (a) if the spin state of the NV_i^- center is $|-\rangle(|+\rangle)$, the photon's polarization state is flipped (unchanged); (b) if the photon's polarization state is $|V\rangle$ ($|H\rangle$), the spin state of the NV_i^- center is flipped (unchanged).

3.3. N_i unit

For the N_i unit illustrated in figure 1(c), assuming the initial states of the NV_i^- center and input photon are the same as the M_i unit. The $|H\rangle$-polarized photon, transmitted by the left-side PBS, sequentially passes through the X, I_i unit, and another X. Meanwhile, the $|V\rangle$-polarized photon, reflected by the left-side PBS, only passes through the WFC before merging with the $|H\rangle$-polarized photon at the right-side PBS. After this process, if the D of I_i unit is not triggered, the hybrid state of the system is evolved into

$$\begin{aligned}
&|H\rangle|+\rangle_i \to r_-(\Delta)|H\rangle|+\rangle_i,\\
&|H\rangle|-\rangle_i \to -r_-(\Delta)|H\rangle|-\rangle_i,\\
&|V\rangle|+\rangle_i \to r_-(\Delta)|V\rangle|+\rangle_i,\\
&|V\rangle|-\rangle_i \to r_-(\Delta)|V\rangle|-\rangle_i.
\end{aligned} \tag{12}$$

Obviously, the function of N_i unit is the exact opposite of the function of M_i unit. Further, if before and after the input photon interacts with the M_i unit, the electron spin of the NV_i^- center of the M_i unit executes Hadamard operation H_i^e, this modification (H^e →interaction with N_i unit→H^e) results in the hybrid state of the system without D triggered evolving into

$$\begin{aligned}
&|H\rangle|+\rangle_i \to r_-(\Delta)|H\rangle|-\rangle_i,\\
&|H\rangle|-\rangle_i \to r_-(\Delta)|H\rangle|+\rangle_i,\\
&|V\rangle|+\rangle_i \to r_-(\Delta)|V\rangle|+\rangle_i,\\
&|V\rangle|-\rangle_i \to r_-(\Delta)|V\rangle|-\rangle_i.
\end{aligned} \tag{13}$$

Equation (13) realizes the desired functionality of the N_i unit. If and only if the photon's polarization is $|H\rangle$, the electron-spin state of the NV_i^- center is flipped.

The three error-predicted units, i.e. I_i, M_i, N_i, described here can be used to construct error-predicted high-dimensional CNOT and Toffoli gates below, playing a crucial role in the simplification of the quantum circuits.

4. 4 × 4-dimensional CNOT gate

So far, we have successfully designed the error-heralded units, denoted as I_i, M_i, and N_i units. In this section, we provide a comprehensive description of the protocol for implementing an error-heralded hybrid 2-qudit CNOT gate within a 4×4-dimensional Hilbert space. The operational principle of the high-dimensional CNOT gate is defined as $U^4_{\mathrm{CNOT}}|c,t\rangle = |c,(t+c)\%\hat{4}\rangle$, where $c,t\in\{\hat{0},\hat{1},\hat{2},\hat{3}\}$. Here, c represents the control qudit, while t represents the target qudit. The four-dimensional control qudit of the CNOT gate is encoded in the hybrid polarization-spatial state of a single photon A, as follows

$$|Ha_1\rangle \to |\hat{0}\rangle_c,\quad |Va_1\rangle \to |\hat{1}\rangle_c,\quad |Ha_2\rangle \to |\hat{2}\rangle_c,\quad |Va_2\rangle \to |\hat{3}\rangle_c, \tag{14}$$

where a_1 and a_2 represent two spatial states of the single photon. Simultaneously, the four-dimensional target qudit is encoded in the electron-spin states of two NV_1^- and NV_2^- centers as

$$\begin{aligned}
&|--\rangle_{12} \to |\hat{0}\rangle_t,\quad |-+\rangle_{12} \to |\hat{1}\rangle_t,\\
&|+-\rangle_{12} \to |\hat{2}\rangle_t,\quad |++\rangle_{12} \to |\hat{3}\rangle_t.
\end{aligned} \tag{15}$$

Considering that control and target qudits are initially prepared in arbitrary states $|\phi\rangle_c$ and $|\phi\rangle_t$, respectively, i.e.

$$\begin{aligned}
|\phi\rangle_c &= \alpha_1|Ha_1\rangle + \alpha_2|Va_1\rangle + \alpha_3|Ha_2\rangle + \alpha_4|Va_2\rangle\\
&= \alpha_1|\hat{0}\rangle_c + \alpha_2|\hat{1}\rangle_c + \alpha_3|\hat{2}\rangle_c + \alpha_4|\hat{3}\rangle_c,\\
|\phi\rangle_t &= \beta_1|--\rangle_{12} + \beta_2|-+\rangle_{12} + \beta_3|+-\rangle_{12} + \beta_4|++\rangle_{12}\\
&= \beta_1|\hat{0}\rangle_t + \beta_2|\hat{1}\rangle_t + \beta_3|\hat{2}\rangle_t + \beta_4|\hat{3}\rangle_t,
\end{aligned} \tag{16}$$

where the coefficients are required to satisfy the normalization condition $|A_1|^2+|A_2|^2+|A_3|^2+|A_4|^2=1$ ($A=\alpha,\beta$). The construction of a high-dimensional CNOT gate necessitates the accurate classification of control qudits and precise tuning of target qudits. We will subsequently detail the four steps involved in both processes.

Firstly, as illustrated in figure 2, the single photon in the spatial modes a_1 and a_2 encounters the leftmost PBSs, splitting the spatial modes of the photon into four distinct spatial modes: a_{11}, a_{12}, a_{21}, and a_{22}. The splitting, governed by the photon's polarization states, initiates the preliminary classification of the four control qudits. Subsequently, before and after the input photon in spatial modes a_{12} and a_{22} interacts with the NV_2^- center of I_2 unit, the electron spin of the NV_2^- center of the I_2 unit executes Hadamard operation H_2^e, that is, H_2^e → interaction with I_2 unit→H_2^e. Meanwhile, the input photon in the spatial modes a_{11} and a_{21} passes through respective WFC. According to the rules specified in equation (8), the initial state $|\Psi_0\rangle = |\phi\rangle_c\otimes|\phi\rangle_t$ of the hybrid system is converted into

$$\begin{aligned}
|\Psi_1\rangle = r_-(\Delta)[&(\alpha_1|Ha_{11}\rangle + \alpha_3|Ha_{21}\rangle)\otimes|\varphi\rangle_t\\
&+(\alpha_2|Va_{12}\rangle + \alpha_4|Va_{22}\rangle)\otimes(\beta_1|-+\rangle_{12}\\
&+\beta_2|--\rangle_{12} + \beta_3|++\rangle_{12} + \beta_4|+-\rangle_{12})].
\end{aligned} \tag{17}$$

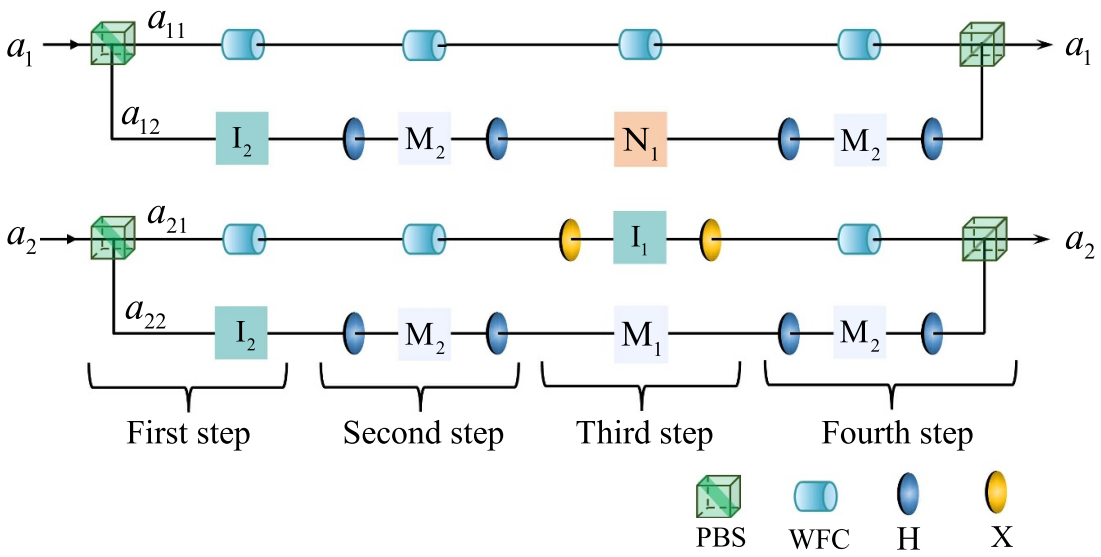

Figure 2. Schematic diagram of the high-dimensional CNOT gate.

In evidence, when the control qudit is in the state $|Va_{12}\rangle$ or $|Va_{22}\rangle$, the electron-spin state of the NV_2^- center of target qudit is flipped, $|-\rangle_2 \leftrightarrow |+\rangle_2$.

Secondly, before and after the photon in spatial modes a_{12} and a_{22} interacts with the NV_2^- center of M_2 unit, the Hadamard operations H^p with left and right Hs are applied to the photon, that is, $H^p \rightarrow$ interaction with M_2 unit$\rightarrow H^p$. Meanwhile, the photon in the spatial modes a_{11} and a_{21} passes through respective WFC. Consequently, by virtue of the rules specified in equation (10), the entire system transitions into the new state

$$\begin{aligned}|\Psi_2\rangle = r_-(\Delta)^2 [&(\alpha_1|Ha_{11}\rangle + \alpha_3|Ha_{21}\rangle) \otimes |\varphi\rangle_t \\ &+ (\alpha_2|Va_{12}\rangle + \alpha_4|Va_{22}\rangle) \otimes (\beta_1|-+\rangle_{12} + \beta_3|++\rangle_{12}) \\ &+ (\alpha_2|Ha_{12}\rangle + \alpha_4|Ha_{22}\rangle) \otimes (\beta_2|--\rangle_{12} + \beta_4|+-\rangle_{12})] .\end{aligned} \tag{18}$$

Obviously, when the spin state of the NV_2^- center of target qudit is $|-\rangle_2$, the polarization state of the control qudit in the spatial modes a_{12} and a_{22} is flipped, $|V\rangle \rightarrow |H\rangle$.

Thirdly, the photon in spatial mode a_{11} passes through the WFC, the photon in spatial modes a_{12} and a_{22} directly interacts with the NV_1^- center of the N_1 unit and the M_1 unit, respectively, and the photon in spatial mode a_{21} passes through a series of operations: X$\rightarrow$ interaction with I_1 unit$\rightarrow$ another X. Before and after these operations, the electron spin of the NV_1^- center undergoes Hadamard operation H_1^e. As a result of the photon-NV_1^- center interactions, the state is transformed into

$$\begin{aligned}|\Psi_3\rangle = r_-(\Delta)^3 [&\alpha_1|Ha_{11}\rangle \otimes |\varphi\rangle_t \\ &+ \alpha_2|Va_{12}\rangle \otimes (\beta_1|-+\rangle_{12} + \beta_3|++\rangle_{12}) \\ &+ \alpha_2|Ha_{12}\rangle \otimes (\beta_2|+-\rangle_{12} + \beta_4|--\rangle_{12}) \\ &+ \alpha_3|Ha_{21}\rangle \otimes (\beta_1|+-\rangle_{12} + \beta_2|++\rangle_{12} + \beta_3|--\rangle_{12} + \beta_4|-+\rangle_{12}) \\ &+ \alpha_4|Va_{22}\rangle \otimes (\beta_1|++\rangle_{12} + \beta_3|-+\rangle_{12}) \\ &+ \alpha_4|Ha_{22}\rangle \otimes (\beta_2|--\rangle_{12} + \beta_4|+-\rangle_{12})] .\end{aligned} \tag{19}$$

Through the step, precise control over the target qudit is achieved.

Fourthly, after the photon undergoes the same operation as the second step, the spatial modes a_{11} and a_{12}, along with a_{21} and a_{22}, are merged into the designated spatial modes a_1 and a_2 using the rightmost PBSs, leading to the modification of equation (19) to

$$\begin{aligned}|\Psi_4\rangle = r_-(\Delta)^4 [&\alpha_1|Ha_1\rangle \otimes |\varphi\rangle_t \\ &+ \alpha_2|Va_1\rangle \otimes (\beta_1|-+\rangle_{12} + \beta_2|+-\rangle_{12} + \beta_3|++\rangle_{12} + \beta_4|--\rangle_{12}) \\ &+ \alpha_3|Ha_2\rangle \otimes (\beta_1|+-\rangle_{12} + \beta_2|++\rangle_{12} + \beta_3|--\rangle_{12} + \beta_4|-+\rangle_{12}) \\ &+ \alpha_4|Va_2\rangle \otimes (\beta_1|++\rangle_{12} + \beta_2|--\rangle_{12} + \beta_3|-+\rangle_{12} + \beta_4|+-\rangle_{12})]\end{aligned}$$

$$
\begin{aligned}
&= r_-(\Delta)^4\left[\alpha_1|\hat{0}\rangle_c\otimes\left(\beta_1|\hat{0}\rangle_t+\beta_2|\hat{1}\rangle_t+\beta_3|\hat{2}\rangle_t+\beta_4|\hat{3}\rangle_t\right)\right.\\
&\quad+\alpha_2|\hat{1}\rangle_c\otimes\left(\beta_1|\hat{1}\rangle_t+\beta_2|\hat{2}\rangle_t+\beta_3|\hat{3}\rangle_t+\beta_4|\hat{0}\rangle_t\right)\\
&\quad+\alpha_3|\hat{2}\rangle_c\otimes\left(\beta_1|\hat{2}\rangle_t+\beta_2|\hat{3}\rangle_t+\beta_3|\hat{0}\rangle_t+\beta_4|\hat{1}\rangle_t\right)\\
&\quad\left.+\alpha_4|\hat{3}\rangle_c\otimes\left(\beta_1|\hat{3}\rangle_t+\beta_2|\hat{0}\rangle_t+\beta_3|\hat{1}\rangle_t+\beta_4|\hat{2}\rangle_t\right)\right]\\
&= r_-(\Delta)^4\left(\alpha_1|\hat{0}\rangle_c X_4^0+\alpha_2|\hat{1}\rangle_c X_4^1+\alpha_3|\hat{2}\rangle_c X_4^2+\alpha_4|\hat{3}\rangle_c X_4^\dagger\right)|\phi\rangle_t,
\end{aligned}
\tag{20}
$$

where X_4^0 represents no operation and the X_4^1, X_4^2, and $X_4^\dagger$ represent three four-dimensional single-qudit operations on the target qudit. The four-dimensional X_4^1 and X_4^2 gates introduce the clockwise cycle operations: $X_4^1|l\rangle=|(l+\hat{1})\%\hat{4}\rangle$ and $X_4^2|l\rangle=|(l+\hat{2})\%\hat{4}\rangle$ ($l=\hat{0},\hat{1},\hat{2},\hat{3}$), effectively shifting each target qudit to its first- and second-nearest counterparts, respectively. Conversely, the $X_4^\dagger$ gate, i.e. $|l\rangle=|(l-\hat{1})\%\hat{4}\rangle$, effects the shift in the counterclockwise direction. Their matrix representations are

$$
\begin{aligned}
X_4^0&=\begin{bmatrix}1&0&0&0\\0&1&0&0\\0&0&1&0\\0&0&0&1\end{bmatrix},\quad X_4^1=\begin{bmatrix}0&1&0&0\\0&0&1&0\\0&0&0&1\\1&0&0&0\end{bmatrix},\\
X_4^2&=\begin{bmatrix}0&0&1&0\\0&0&0&1\\1&0&0&0\\0&1&0&0\end{bmatrix},\quad X_4^\dagger=\begin{bmatrix}0&0&0&1\\1&0&0&0\\0&1&0&0\\0&0&1&0\end{bmatrix}.
\end{aligned}
\tag{21}
$$

After completing the aforementioned four steps, we have successfully modulated the target qudit to the desired state and finalized the design of the high-dimensional CNOT gate, corresponding matrix representation with the specified 16 basis expressed as

$$
\mathrm{CNOT}=\begin{bmatrix}X_4^0&0&0&0\\0&X_4^1&0&0\\0&0&X_4^2&0\\0&0&0&X_4^\dagger\end{bmatrix}.
\tag{22}
$$

5. $4\times4\times4$-dimensional Toffoli gate

Next, we present a comprehensive description for implementing an error-heralded hybrid 3-qudit Toffoli gate within a $4\times4\times4$-dimensional Hilbert space. The operational principle of the high-dimensional Toffoli gate is articulated as $U_{\mathrm{Toffoli}}^4|c_1,c_2,t\rangle=|c_1,c_2,(t+c_1*c_2)\%\hat{4}\rangle$, where $c_1,c_2,t\in\{\hat{0},\hat{1},\hat{2},\hat{3}\}$. Here, c_1 and c_2 denote the first and second control qudits, respectively, while t signifies the target qudit. The first four-dimensional control qudit of the high-dimensional Toffoli gate is encoded in the polarization-spatial states of the single photon B, i.e.

$$
|Hb_1\rangle\rightarrow|\hat{0}\rangle_{c_1},\quad |Hb_2\rangle\rightarrow|\hat{1}\rangle_{c_1},\quad |Vb_1\rangle\rightarrow|\hat{2}\rangle_{c_1},\quad |Vb_2\rangle\rightarrow|\hat{3}\rangle_{c_1}.
\tag{23}
$$

Simultaneously, the second control qudit is encoded in the electron-spin states of two NV_3^- and NV_4^- centers, i.e.

$$
\begin{aligned}
|--\rangle_{34}\rightarrow|\hat{0}\rangle_{c_2},\quad |-+\rangle_{34}\rightarrow|\hat{1}\rangle_{c_2},\\
|+-\rangle_{34}\rightarrow|\hat{2}\rangle_{c_2},\quad |++\rangle_{34}\rightarrow|\hat{3}\rangle_{c_2}.
\end{aligned}
\tag{24}
$$

The four-dimensional target qudit is also encoded in the electron-spin states of two NV_5^- and NV_6^- centers, i.e.

$$
\begin{aligned}
|--\rangle_{56}\rightarrow|\hat{0}\rangle_t,\quad |-+\rangle_{56}\rightarrow|\hat{1}\rangle_t,\\
|+-\rangle_{56}\rightarrow|\hat{2}\rangle_t,\quad |++\rangle_{56}\rightarrow|\hat{3}\rangle_t.
\end{aligned}
\tag{25}
$$

Assuming that the initial entanglements of four NV^- centers and the photon B are arbitrary, denoted as

$$
\begin{aligned}
|\varphi\rangle_{c_1}&=\mu_1|Hb_1\rangle+\mu_2|Hb_2\rangle+\mu_3|Vb_1\rangle+\mu_4|Vb_2\rangle\\
&=\mu_1|\hat{0}\rangle_{c_1}+\mu_2|\hat{1}\rangle_{c_1}+\mu_3|\hat{2}\rangle_{c_1}+\mu_4|\hat{3}\rangle_{c_1},\\
|\varphi\rangle_{c_2}&=\nu_1|--\rangle_{34}+\nu_2|-+\rangle_{34}+\nu_3|+-\rangle_{34}+\nu_4|++\rangle_{34}
\end{aligned}
$$

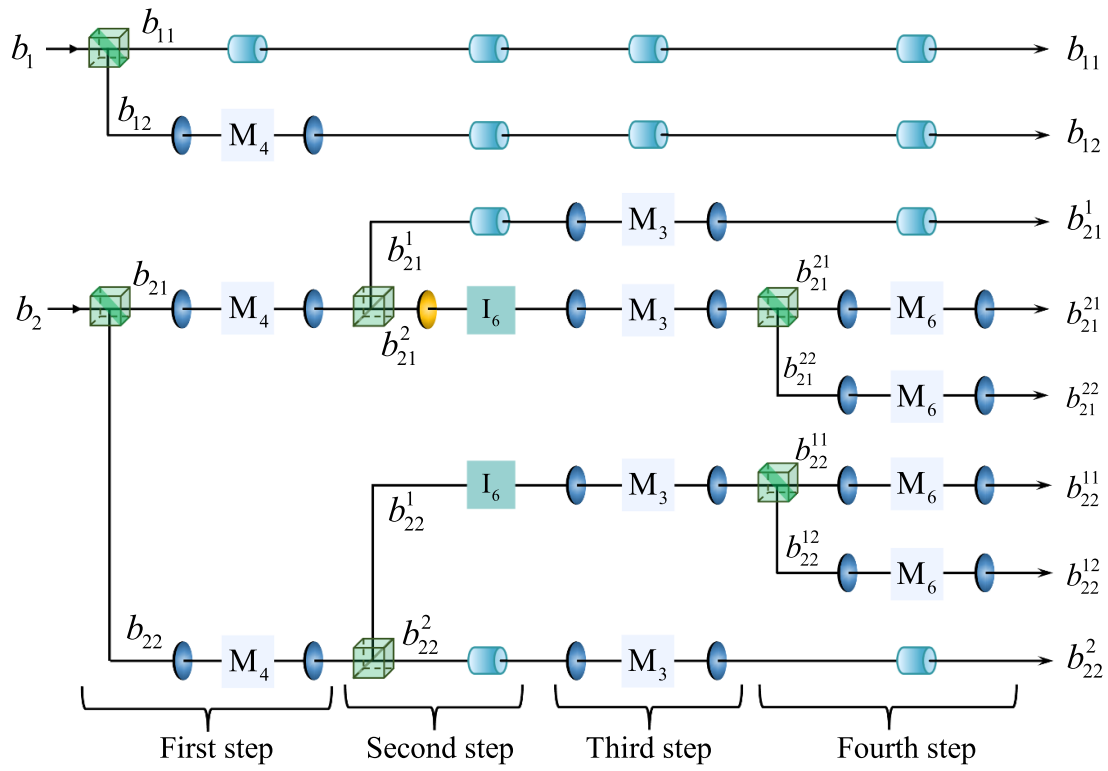

Figure 3. Schematic diagram of the accurate classification and coarse tuning of the high-dimensional Toffoli gate.

$$
\begin{aligned}
&= \nu_1|\hat{0}\rangle_{c_2} + \nu_2|\hat{1}\rangle_{c_2} + \nu_3|\hat{2}\rangle_{c_2} + \nu_4|\hat{3}\rangle_{c_2},\\
|\varphi\rangle_t &= \xi_1|--\rangle_{56} + \xi_2|-+\rangle_{56} + \xi_3|+-\rangle_{56} + \xi_4|++\rangle_{56}\\
&= \xi_1|\hat{0}\rangle_t + \xi_2|\hat{1}\rangle_t + \xi_3|\hat{2}\rangle_t + \xi_4|\hat{3}\rangle_t,
\end{aligned} \tag{26}
$$

where the coefficients satisfy the normalization condition $|K_1|^2 + |K_2|^2 + |K_3|^2 + |K_4|^2 = 1$, $(K = \mu, \nu, \xi)$. The construction of the high-dimensional Toffoli gate unfolds in eight steps provided in figures 3 and 4, as detailed below, where the four steps are involved in each process. The figure 3 sets up precise classification for control qudits and coarse tuning for target qudits. The figure 4 conducts more precise operation on the target qudit and merges the previously split spatial modes, effectively implementing the high-dimensional Toffoli gate.

5.1. Accurate classification and coarse tuning

Firstly, as depicted in figure 3, photon B traveling along spatial modes b_1 and b_2 passes through the leftmost PBSs, resulting in a split into four distinct spatial modes: b_{11}, b_{12}, b_{21}, and b_{22}. This division, dictated by the photon's polarization state, finalizes the preliminary classification of the first control qudit. Then photon B in spatial mode b_1 directly passes through the WFC, simultaneously, before and after photon B in spatial modes b_{12}, b_{21}, and b_{22} interacts with the NV_4^- center of M_4 unit, the Hadamard operations H^p with left and right Hs are applied to photon B, that is, H^p $\rightarrow$ interaction with M_4 unit$\rightarrow H^p$. By the rules in equation (10), the initial state $|\Phi_0\rangle = |\varphi\rangle_{c_1} \otimes |\varphi\rangle_{c_2} \otimes |\varphi\rangle_t$ of the hybrid system is converted into

$$
\begin{aligned}
|\Phi_1\rangle = r_-(\Delta)\,[&\mu_1|Hb_{11}\rangle \otimes |\varphi\rangle_{c_2}\\
&+ (\mu_2|Hb_{21}\rangle + \mu_3|Vb_{12}\rangle + \mu_4|Vb_{22}\rangle) \otimes (\nu_2|-+\rangle_{34} + \nu_4|++\rangle_{34})\\
&+ (\mu_2|Vb_{21}\rangle + \mu_3|Hb_{12}\rangle + \mu_4|Hb_{22}\rangle) \otimes (\nu_1|--\rangle_{34} + \nu_3|+-\rangle_{34})]\\
&\otimes |\varphi\rangle_t.
\end{aligned} \tag{27}
$$

Secondly, photon B traveling along spatial modes b_{21} and b_{22} passes through the intermediate PBSs, resulting in a division into four spatial modes: b_{21}^1, b_{21}^2, b_{22}^1, and b_{22}^2. Then photon B in spatial modes b_{11}, b_{12}, b_{21}^1, and b_{22}^2 directly passes through the respective WFC, simultaneously, before and after photon B in spatial modes b_{21}^2 (traversing X) and b_{22}^1 interacts with the NV_6^- center of I_6 unit, the Hadamard operation H_6^e is executed on the electron spin of the NV_6^- center, that is, H_6^e $\rightarrow$ interaction with I_6 unit$\rightarrow H_6^e$. Following the

procedure, the state of the entire system is transformed into

$$
\begin{aligned}
|\Phi_2\rangle = r_-(\Delta)^2 \{ & [\mu_1|Hb_{11}\rangle \otimes |\varphi\rangle_{c_2} + \left(\mu_2|Vb_{21}^1\rangle + \mu_3|Hb_{12}\rangle + \mu_4|Hb_{22}^2\rangle\right) \\
& \otimes (\nu_1|--\rangle_{34} + \nu_3|+-\rangle_{34}) \\
& + \mu_3|Vb_{12}\rangle \otimes (\nu_2|-+\rangle_{34} + \nu_4|++\rangle_{34})] \otimes |\varphi\rangle_t \\
& + \left(\mu_2|Vb_{21}^2\rangle + \mu_4|Vb_{22}^1\rangle\right) \otimes (\nu_2|-+\rangle_{34} + \nu_4|++\rangle_{34}) \\
& \otimes (\xi_1|-+\rangle_{56} + \xi_2|--\rangle_{56} + \xi_3|++\rangle_{56} + \xi_4|+-\rangle_{56})\}.
\end{aligned} \tag{28}
$$

In evidence, if and only if the control qudit is in the $|Vb_{21}^2\rangle$ or $|Vb_{22}^1\rangle$, the electron-spin state of the NV center of target qudit is flipped, $|-\rangle_6 \leftrightarrow |+\rangle_6$.

Thirdly, photon B in spatial modes b_{11} and b_{12} directly passes through respective WFC, simultaneously, before and after photon B in other spatial modes b_{21}^1, b_{21}^2, b_{22}^1, and b_{22}^2 interacts with the NV_3^- center of M_3 unit, the Hadamard operations H^p with left and right Hs are applied to photon B, that is, $H^p \rightarrow$ interaction with M_3 unit$\rightarrow H^p$. By the rules in equation (10), resulting in the state of the hybrid system

$$
\begin{aligned}
|\Phi_3\rangle = r_-(\Delta)^3 \{ & [\mu_1|Hb_{11}\rangle \otimes |\varphi\rangle_{c_2} + \left(\mu_2|Hb_{21}^1\rangle + \mu_3|Hb_{12}\rangle + \mu_4|Vb_{22}^2\rangle\right) \\
& \otimes \nu_1|--\rangle_{34} + \left(\mu_2|Vb_{21}^1\rangle + \mu_3|Hb_{12}\rangle + \mu_4|Hb_{22}^2\rangle\right) \otimes \nu_3|+-\rangle_{34} \\
& + \mu_3|Vb_{12}\rangle \otimes (\nu_2|-+\rangle_{34} + \nu_4|++\rangle_{34})] \otimes |\varphi\rangle_t + \left[\left(\mu_2|Hb_{21}^2\rangle\right.\right. \\
& \left.\left. + \mu_4|Hb_{22}^1\rangle\right) \otimes \nu_2|-+\rangle_{34} + \left(\mu_2|Vb_{21}^2\rangle + \mu_4|Vb_{22}^1\rangle\right) \otimes \nu_4|++\rangle_{34}\right] \\
& \otimes (\xi_1|-+\rangle_{56} + \xi_2|--\rangle_{56} + \xi_3|++\rangle_{56} + \xi_4|+-\rangle_{56})\}.
\end{aligned} \tag{29}
$$

At this juncture, we have successfully classified for the two control qudits. This classification is essential for executing subsequent operations on the target qudit, contingent upon the various combinations of control qudits.

Fourthly, photon B traveling along spatial modes b_{21}^2 and b_{22}^1 passes through the rightmost PBSs, splitting into four spatial modes again: b_{21}^{21}, b_{21}^{22}, b_{22}^{11}, and b_{22}^{12}. Then photon B in spatial modes b_{11}, b_{12}, b_{21}^1, and b_{22}^2 directly passes through the respective WFC, simultaneously, before and after photon B in spatial modes b_{21}^{21}, b_{21}^{22}, b_{22}^{11}, and b_{22}^{12} interacts with the NV_6^- center of M_6 unit, Hadamard operations H^p with left and right Hs are applied to photon B, that is, $H^p \rightarrow$ interaction with M_6 unit$\rightarrow H^p$. By the rules in equation (10), the state of $|\Phi_3\rangle$ evolves into

$$
\begin{aligned}
|\Phi_4\rangle = r_-(\Delta)^4 \{ & [(\mu_1|Hb_{11}\rangle \otimes |\varphi\rangle_{c_2} + (\mu_2|Hb_{21}^1\rangle + \mu_3|Hb_{12}\rangle + \mu_4|Vb_{22}^2\rangle) \\
& \otimes \nu_1|--\rangle_{34} + (\mu_2|Vb_{21}^1\rangle + \mu_3|Hb_{12}\rangle + \mu_4|Hb_{22}^2\rangle) \otimes \nu_3|+-\rangle_{34} \\
& + \mu_3|Vb_{12}\rangle \otimes (\nu_2|-+\rangle_{34} + \nu_4|++\rangle_{34})] \otimes |\varphi\rangle_t + [(\mu_2|Hb_{21}^{21}\rangle \\
& + \mu_4|Hb_{22}^{11}\rangle) \otimes \nu_2|-+\rangle_{34} + (\mu_2|Vb_{21}^{22}\rangle + \mu_4|Vb_{22}^{12}\rangle) \otimes \nu_4|++\rangle_{34}] \\
& \otimes (\xi_1|-+\rangle_{56} + \xi_3|++\rangle_{56}) + [(\mu_2|Vb_{21}^{21}\rangle + \mu_4|Vb_{22}^{11}\rangle) \otimes \nu_2|-+\rangle_{34} \\
& + (\mu_2|Hb_{21}^{22}\rangle + \mu_4|Hb_{22}^{12}\rangle) \otimes \nu_4|++\rangle_{34}] \otimes (\xi_2|--\rangle_{56} + \xi_4|+-\rangle_{56})\}.
\end{aligned} \tag{30}
$$

An analysis of equation (30) reveals that classification utilizing the electron spin of the NV_6^- center in the target qudit is employed. This division segments the system into eight distinct parts, facilitating more precise manipulation on the specific target qudit.

By implementing the four outlined steps, we have subdivided the initial two spatial modes into eight, achieving precise classification of the two control qudits and making initial adjustments to the target qudit. The subdivision into eight spatial modes enables more precise operations on the target qudit, playing a pivotal role in the construction of the high-dimensional Toffoli gate.

5.2. Precise operation and spatial-mode fusion

As depicted in figure 4, we conduct more precise operations on the target qudit and merge the previously split spatial modes, effectively completely implementing the high-dimensional Toffoli gate. The process is delineated in four distinct steps.

Fifthly, photon B in spatial mode b_{11} passes through the WFC, the photon in spatial modes $b_{12}, b_{21}^1, b_{21}^{21}, b_{21}^{22}$ and $b_{22}^{11}, b_{22}^{12}, b_{22}^2$ interacts with NV_5^- center of the M_5 and N_5 units, respectively. Before and after these operations, the electron spin of the NV_5^- center undergoes Hadamard operation H_5^e. Consequently, the state $|\Phi\rangle_4$ is transformed into

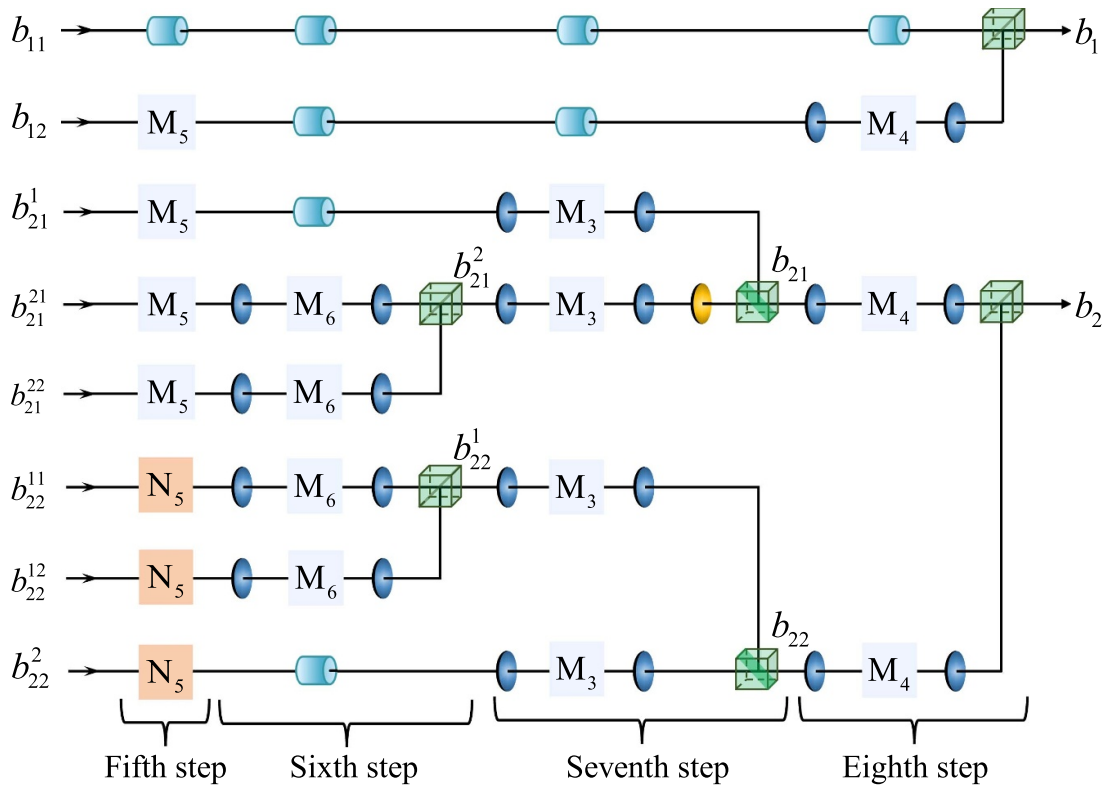

Figure 4. Schematic diagram of the precise operation and spatial-mode fusion of the high-dimensional Toffoli gate.

$$
\begin{aligned}
|\Phi_5\rangle = r_-(\Delta)^5 \{ & [\mu_1|Hb_{11}\rangle \otimes |\varphi\rangle_{c_2} + (\mu_2|Hb_{21}^1\rangle + \mu_4|Vb_{22}^2\rangle) \otimes \nu_1|--\rangle_{34} \\
& + \mu_3|Hb_{12}\rangle (\nu_1|--\rangle_{34} + \nu_3|+-\rangle_{34})] \otimes |\varphi\rangle_t + \mu_2\nu_2|Hb_{21}^{21}\rangle|-+\rangle_{34} \\
& \otimes (\xi_1|-+\rangle_{56} + \xi_3|++\rangle_{56}) + \mu_2\nu_2|Vb_{21}^{21}\rangle|-+\rangle_{34} \\
& \otimes (\xi_2|+-\rangle_{56} + \xi_4|--\rangle_{56}) + \mu_2\nu_4|Vb_{21}^{22}\rangle|++\rangle_{34} \\
& \otimes (\xi_1|++\rangle_{56} + \xi_3|-+\rangle_{56}) + \mu_2\nu_4|Hb_{21}^{22}\rangle|++\rangle_{34} \\
& \otimes (\xi_2|--\rangle_{56} + \xi_4|+-\rangle_{56}) + (\mu_2\nu_3|Vb_{21}^1\rangle|+-\rangle_{34} \\
& + \mu_4\nu_3|Hb_{22}^2\rangle|+-\rangle_{34}) \otimes (\xi_1|+-\rangle_{56} + \xi_2|++\rangle_{56} + \xi_3|--\rangle_{56} \\
& + \xi_4|-+\rangle_{56}) + \mu_3|Vb_{12}\rangle (\nu_2|-+\rangle_{34} + \nu_4|++\rangle_{34}) \otimes (\xi_1|+-\rangle_{56} \\
& + \xi_2|++\rangle_{56} + \xi_3|--\rangle_{56} + \xi_4|-+\rangle_{56}) + \mu_4\nu_2|Hb_{22}^{11}\rangle|-+\rangle_{34} \\
& \otimes (\xi_1|++\rangle_{56} + \xi_3|-+\rangle_{56}) + \mu_4\nu_2|Vb_{22}^{11}\rangle|-+\rangle_{34} \\
& \otimes (\xi_2|--\rangle_{56} + \xi_4|+-\rangle_{56}) + \mu_4\nu_4|Vb_{22}^{12}\rangle|++\rangle_{34} \\
& \otimes (\xi_1|-+\rangle_{56} + \xi_3|++\rangle_{56}) + \mu_4\nu_4|Hb_{22}^{12}\rangle|++\rangle_{34} \\
& \otimes (\xi_2|+-\rangle_{56} + \xi_4|--\rangle_{56})\} . \qquad (31)
\end{aligned}
$$

According to equation (31), the two target spins are transformed into their desired states, thereby completing all necessary precise operations on the target qudits. Subsequently, we merge the eight distinct spatial modes b_{11}, b_{12}, b_{21}^1, b_{21}^{21}, b_{21}^{22}, b_{22}^{11}, b_{22}^{12}, and b_{22}^2 into the original two spatial modes denoted as b_1 and b_2, through the following three steps.

Sixthly, after photon B undergoes the same operation as the fourth step, by the help of the leftmost PBSs, the spatial modes b_{21}^{21} and b_{21}^{22}, along with b_{22}^{11} and b_{22}^{12}, are merged into the designated spatial modes b_{21}^2 and b_{22}^1, respectively, resulting in

$$
\begin{aligned}
|\Phi_6\rangle = r_-(\Delta)^6 \{ & [\mu_1|Hb_{11}\rangle \otimes |\varphi\rangle_{c_2} + (\mu_2|Hb_{21}^1\rangle + \mu_4|Vb_{22}^2\rangle) \otimes \nu_1|--\rangle_{34} \\
& + \mu_3|Hb_{12}\rangle (\nu_1|--\rangle_{34} + \nu_3|+-\rangle_{34})] \otimes |\varphi\rangle_t + (\mu_2\nu_2|Hb_{21}^2\rangle|-+\rangle_{34} \\
& + \mu_4\nu_4|Vb_{22}^1\rangle|++\rangle_{34}) \otimes (\xi_1|-+\rangle_{56} + \xi_2|+-\rangle_{56} + \xi_3|++\rangle_{56} \\
& + \xi_4|--\rangle_{56}) + (\mu_2\nu_4|Vb_{21}^2\rangle|++\rangle_{34} + \mu_4\nu_2|Hb_{22}^1\rangle|-+\rangle_{34}) \\
& \otimes (\xi_1|++\rangle_{56} + \xi_2|--\rangle_{56} + \xi_3|-+\rangle_{56} + \xi_4|+-\rangle_{56})
\end{aligned}
$$

$$
\begin{aligned}
&+\left(\mu_2\nu_3|Vb_{21}^1\rangle|+-\rangle_{34}+\mu_4\nu_3|Hb_{22}^2\rangle|+-\rangle_{34}\right)\\
&\otimes\left(\xi_1|+-\rangle_{56}+\xi_2|++\rangle_{56}+\xi_3|--\rangle_{56}+\xi_4|-+\rangle_{56}\right)\\
&+\mu_3|Vb_{12}\rangle\left(\nu_2|-+\rangle_{34}+\nu_4|++\rangle_{34}\right)\\
&\otimes\left(\xi_1|+-\rangle_{56}+\xi_2|++\rangle_{56}+\xi_3|--\rangle_{56}+\xi_4|-+\rangle_{56}\right)\}. \qquad (32)
\end{aligned}
$$

Seventhly, after photon B undergoes the same operation as the third step and photon B in spatial mode b_{21}^2 undergoes X, the spatial modes b_{21}^1 and b_{21}^2, along with b_{22}^1, and b_{22}^2, are integrated into the designated spatial modes b_{21} and b_{22}, respectively, using the intermediate PBSs, which facilitates the system's evolution into

$$
\begin{aligned}
|\Phi_7\rangle = r_-(\Delta)^7\{&[\mu_1|Hb_{11}\rangle\otimes|\varphi\rangle_{c_2}+(\mu_2|Vb_{21}\rangle+\mu_4|Hb_{22}\rangle)\\
&\otimes\nu_1|--\rangle_{34}+\mu_3|Hb_{12}\rangle(\nu_1|--\rangle_{34}+\nu_3|+-\rangle_{34})]\\
&\otimes|\varphi\rangle_t+(\mu_2\nu_2|Hb_{21}\rangle|-+\rangle_{34}+\mu_4\nu_4|Vb_{22}\rangle|++\rangle_{34})\\
&\otimes(\xi_1|-+\rangle_{56}+\xi_2|+-\rangle_{56}+\xi_3|++\rangle_{56}+\xi_4|--\rangle_{56})\\
&+(\mu_2\nu_4|Hb_{21}\rangle|++\rangle_{34}+\mu_4\nu_2|Vb_{22}\rangle|-+\rangle_{34})\\
&\otimes(\xi_1|++\rangle_{56}+\xi_2|--\rangle_{56}+\xi_3|-+\rangle_{56}+\xi_4|+-\rangle_{56})\\
&+(\mu_2\nu_3|Vb_{21}\rangle|+-\rangle_{34}+\mu_4\nu_3|Hb_{22}\rangle|+-\rangle_{34})\\
&\otimes(\xi_1|+-\rangle_{56}+\xi_2|++\rangle_{56}+\xi_3|--\rangle_{56}+\xi_4|-+\rangle_{56})\\
&+\mu_3|Vb_{12}\rangle(\nu_2|-+\rangle_{34}+\nu_4|++\rangle_{34})\\
&\otimes(\xi_1|+-\rangle_{56}+\xi_2|++\rangle_{56}+\xi_3|--\rangle_{56}+\xi_4|-+\rangle_{56})\}. \qquad (33)
\end{aligned}
$$

Eighthly, after photon B undergoes the same operation as the first step, the spatial modes b_{11} and b_{12}, along with b_{21} and b_{22}, are consolidated into the designated spatial modes b_1 and b_2, respectively, by the rightmost PBSs, leading to the modification of equation (33) to

$$
\begin{aligned}
|\Phi_8\rangle = r_-(\Delta)^8\{&[\mu_1|Hb_1\rangle\otimes|\varphi\rangle_{c_2}+\mu_2\nu_1|Hb_2\rangle|--\rangle_{34}+\mu_3|Vb_1\rangle\\
&\otimes(\nu_1|--\rangle_{34}+\nu_3|+-\rangle_{34})+\mu_4\nu_1|Vb_2\rangle|--\rangle_{34}]\otimes|\varphi\rangle_t\\
&+(\mu_2\nu_2|Hb_2\rangle|-+\rangle_{34}+\mu_4\nu_4|Vb_2\rangle|++\rangle_{34})\\
&\otimes(\xi_1|-+\rangle_{56}+\xi_2|+-\rangle_{56}+\xi_3|++\rangle_{56}+\xi_4|--\rangle_{56})\\
&+(\mu_2\nu_3|Hb_2\rangle|+-\rangle_{34}+\mu_4\nu_3|Vb_2\rangle|+-\rangle_{34})\\
&\otimes(\xi_1|+-\rangle_{56}+\xi_2|++\rangle_{56}+\xi_3|--\rangle_{56}+\xi_4|-+\rangle_{56})\\
&+(\mu_2\nu_4|Hb_2\rangle|++\rangle_{34}+\mu_4\nu_2|Vb_2\rangle|-+\rangle_{34})\\
&\otimes(\xi_1|++\rangle_{56}+\xi_2|--\rangle_{56}+\xi_3|-+\rangle_{56}+\xi_4|+-\rangle_{56})\\
&+\mu_3|Vb_1\rangle(\nu_2|-+\rangle_{34}+\nu_4|++\rangle_{34})\\
&\otimes(\xi_1|+-\rangle_{56}+\xi_2|++\rangle_{56}+\xi_3|--\rangle_{56}+\xi_4|-+\rangle_{56})\}. \qquad (34)
\end{aligned}
$$

Based on the encoded input state $|\Phi_0\rangle$, $|\Phi_8\rangle$ is expressed as

$$
\begin{aligned}
|\Phi_8'\rangle = r_-(\Delta)^8\{&\left[\mu_1|\hat{0}\rangle_{c_1}\otimes\left(\nu_1|\hat{0}\rangle_{c_2}+\nu_1|\hat{1}\rangle_{c_2}+\nu_2|\hat{2}\rangle_{c_2}+\nu_4|\hat{3}\rangle_{c_2}\right)\right.\\
&\left.+\nu_1\left(\mu_2|\hat{1}\rangle_{c_1}+\mu_3|\hat{2}\rangle_{c_1}+\mu_4|\hat{3}\rangle_{c_1}\right)|\hat{0}\rangle_{c_2}+\mu_3\nu_3|\hat{2}\rangle_{c_1}|\hat{2}\rangle_{c_2}\right]\\
&\otimes\left(\xi_1|\hat{0}\rangle_t+\xi_1|\hat{1}\rangle_t+\xi_2|\hat{2}\rangle_t+\xi_4|\hat{3}\rangle_t\right)\\
&+\left(\mu_2\nu_2|\hat{1}\rangle_{c_1}|\hat{1}\rangle_{c_2}+\mu_4\nu_4|\hat{3}\rangle_{c_1}|\hat{3}\rangle_{c_2}\right)\\
&\otimes\left(\xi_1|\hat{1}\rangle_t+\xi_2|\hat{2}\rangle_t+\xi_3|\hat{3}\rangle_t+\xi_4|\hat{0}\rangle_t\right)\\
&+\left(\mu_2\nu_3|\hat{1}\rangle_{c_1}|\hat{2}\rangle_{c_2}+\mu_3\nu_2|\hat{2}\rangle_{c_1}|\hat{1}\rangle_{c_2}+\mu_3\nu_4|\hat{2}\rangle_{c_1}|\hat{3}\rangle_{c_2}+\mu_4\nu_3|\hat{3}\rangle_{c_1}|\hat{2}\rangle_{c_2}\right)\\
&\otimes\left(\xi_1|\hat{2}\rangle_t+\xi_2|\hat{3}\rangle_t+\xi_3|\hat{0}\rangle_t+\xi_4|\hat{1}\rangle_t\right)\\
&+\left(\mu_2\nu_4|\hat{1}\rangle_{c_1}|\hat{3}\rangle_{c_2}+\mu_4\nu_2|\hat{3}\rangle_{c_1}|\hat{1}\rangle_{c_2}\right)\\
&\otimes\left(\xi_1|\hat{3}\rangle_t+\xi_2|\hat{0}\rangle_t+\xi_3|\hat{1}\rangle_t+\xi_4|\hat{2}\rangle_t\right)\}.\\
=r_-(\Delta)^8\{&\left[\mu_1|\hat{0}\rangle_{c_1}\otimes\left(\nu_1|\hat{0}\rangle_{c_2}+\nu_1|\hat{1}\rangle_{c_2}+\nu_2|\hat{2}\rangle_{c_2}+\nu_4|\hat{3}\rangle_{c_2}\right)\right.\\
&\left.+\nu_1\left(\mu_2|\hat{1}\rangle_{c_1}+\mu_3|\hat{2}\rangle_{c_1}+\mu_4|\hat{3}\rangle_{c_1}\right)|\hat{0}\rangle_{c_2}+\mu_3\nu_3|\hat{2}\rangle_{c_1}|\hat{2}\rangle_{c_2}\right]X_4^0
\end{aligned}
$$

$$+\left(\mu_2\nu_2|\hat{1}\rangle_{c_1}|\hat{1}\rangle_{c_2}+\mu_4\nu_4|\hat{3}\rangle_{c_1}|\hat{3}\rangle_{c_2}\right)X_4^1+\left(\mu_2\nu_3|\hat{1}\rangle_{c_1}|\hat{2}\rangle_{c_2}$$
$$+\mu_3\nu_2|\hat{2}\rangle_{c_1}|\hat{1}\rangle_{c_2}+\mu_3\nu_4|\hat{2}\rangle_{c_1}|\hat{3}\rangle_{c_2}+\mu_4\nu_3|\hat{3}\rangle_{c_1}|\hat{2}\rangle_{c_2}\right)X_4^2$$
$$+\left(\mu_2\nu_4|\hat{1}\rangle_{c_1}|\hat{3}\rangle_{c_2}+\mu_4\nu_2|\hat{3}\rangle_{c_1}|\hat{1}\rangle_{c_2}\right)X_4^\dagger\Big\}|\varphi\rangle_t. \quad (35)$$

It is clear that the hybrid $4\times4\times4$-dimensional Toffoli gate, as outlined in equation (35), has been successfully implemented with unity fidelity even under the imperfect NV$^-$-cavity interaction and ignoring photon loss. The corresponding matrix representation of the $4\times4\times4$-dimensional Toffoli gate, with the specified 64 basis, is expressed as

$$\begin{bmatrix}
X_4^0 & 0 & 0 & 0 & 0 & 0 & 0 & 0 & 0 & 0 & 0 & 0 & 0 & 0 & 0 & 0\\
0 & X_4^0 & 0 & 0 & 0 & 0 & 0 & 0 & 0 & 0 & 0 & 0 & 0 & 0 & 0 & 0\\
0 & 0 & X_4^0 & 0 & 0 & 0 & 0 & 0 & 0 & 0 & 0 & 0 & 0 & 0 & 0 & 0\\
0 & 0 & 0 & X_4^0 & 0 & 0 & 0 & 0 & 0 & 0 & 0 & 0 & 0 & 0 & 0 & 0\\
0 & 0 & 0 & 0 & X_4^0 & 0 & 0 & 0 & 0 & 0 & 0 & 0 & 0 & 0 & 0 & 0\\
0 & 0 & 0 & 0 & 0 & X_4^1 & 0 & 0 & 0 & 0 & 0 & 0 & 0 & 0 & 0 & 0\\
0 & 0 & 0 & 0 & 0 & 0 & X_4^2 & 0 & 0 & 0 & 0 & 0 & 0 & 0 & 0 & 0\\
0 & 0 & 0 & 0 & 0 & 0 & 0 & X_4^\dagger & 0 & 0 & 0 & 0 & 0 & 0 & 0 & 0\\
0 & 0 & 0 & 0 & 0 & 0 & 0 & 0 & X_4^0 & 0 & 0 & 0 & 0 & 0 & 0 & 0\\
0 & 0 & 0 & 0 & 0 & 0 & 0 & 0 & 0 & X_4^2 & 0 & 0 & 0 & 0 & 0 & 0\\
0 & 0 & 0 & 0 & 0 & 0 & 0 & 0 & 0 & 0 & X_4^0 & 0 & 0 & 0 & 0 & 0\\
0 & 0 & 0 & 0 & 0 & 0 & 0 & 0 & 0 & 0 & 0 & X_4^2 & 0 & 0 & 0 & 0\\
0 & 0 & 0 & 0 & 0 & 0 & 0 & 0 & 0 & 0 & 0 & 0 & X_4^0 & 0 & 0 & 0\\
0 & 0 & 0 & 0 & 0 & 0 & 0 & 0 & 0 & 0 & 0 & 0 & 0 & X_4^\dagger & 0 & 0\\
0 & 0 & 0 & 0 & 0 & 0 & 0 & 0 & 0 & 0 & 0 & 0 & 0 & 0 & X_4^2 & 0\\
0 & 0 & 0 & 0 & 0 & 0 & 0 & 0 & 0 & 0 & 0 & 0 & 0 & 0 & 0 & X_4^1
\end{bmatrix}. \quad (36)$$

6. Discussion and summary

So far, we have realized deterministic hybrid CNOT and Toffoli gates in 4×4 and $4\times4\times4$ dimensions, respectively, using error-heralded quantum units without the need for auxiliary qubits, where the control qudit is encoded in the spatial-polarization states of one photon, and the target qudit is encoded in the electron-spin states of two NV$^-$ centers. In two protocols, during imperfect photon scattering process, errors from non-ideal scattering three units, i.e. I_i, M_i, N_i of high-dimensional CNOT and Toffoli gates are passively filtered by the PBS. For instance, in equation (7), the PBS passively filters out the incorrect $|V\rangle$ state components while transmitting the useful $|H\rangle$ state components to X. The response of D is solely used to indicate the presence of errors, and its efficiency does not impact the fidelity. As a result, the fidelities of these gates, keeping in error-predicted way, have near unity ignoring photon loss, in principle, but their efficiencies can be impacted.

We mainly focus on discussion on the efficiencies of the high-dimensional CNOT and Toffoli gates. The target qudits of the CNOT and Toffoli gates encode information using electron-spin states within two separate NV$^-$-cavity systems, eliminating the need for auxiliary entangled states or additional qudits. NV$^-$ center offers several advantages over a qudit-based system, including long coherence times (over 10 ms) at room temperature, rapid spin-state manipulation (sub-nanosecond), and fast readout (100 μs) via microwave excitation [82]. The interaction between photons and electron spin is a pivotal aspect of our protocols and can be further enhanced by coupling the NV$^-$ center to a frequency-degenerate cavity. Furthermore, photon-spin hybrid entangled states have been successfully demonstrated for NV$^-$ center system under both strong and weak coupling regimes [92].

The efficiencies for the error-heralded CNOT and Toffoli gates are $\eta_1=r_-(\Delta)^8$ and $\eta_2=r_-(\Delta)^{16}$, respectively, where they are affected by the factor $|r_-(\Delta)|$. Further, according to $|r_-(\Delta)|=\frac{1}{\sqrt{2}}[r(\Delta,0)-r(\Delta,g)]$, the frequency detuning Δ, the cavity-decay rate κ_s/κ, the ratio between coupling strength and decay rate g/κ may involve it. In practical experiments, $\gamma=0.01\kappa$ can be achieved. The efficiencies η_1 and η_2 vs the factor g/κ with the resonant frequency $\Delta=0$ shown in figure 5(a) and the frequency detuning condition $\Delta=\pm g$ shown in figure 5(b) taking the case cavity-decay rate $\kappa_s/\kappa=0$. In evidence, the efficiencies η_1 and η_2 increase significantly as g/κ increases. For instance, in figure 5(a), raising g/κ from 0.70 to 2.40 results in efficiencies improvements from 95.98% and 92.12% to 99.65% and 99.30%, respectively. Furthermore, in the case of $\kappa_s/\kappa=0.01$, figure 5(c) illustrates the relationship between the efficiencies and the factor g/κ at $\Delta=0$, while figure 5(d) shows the relationship between the efficiencies and the factor g/κ at $\Delta=\pm g$. In figure 5(c), raising g/κ from 0.70 to 2.40 results in efficiency improvements for

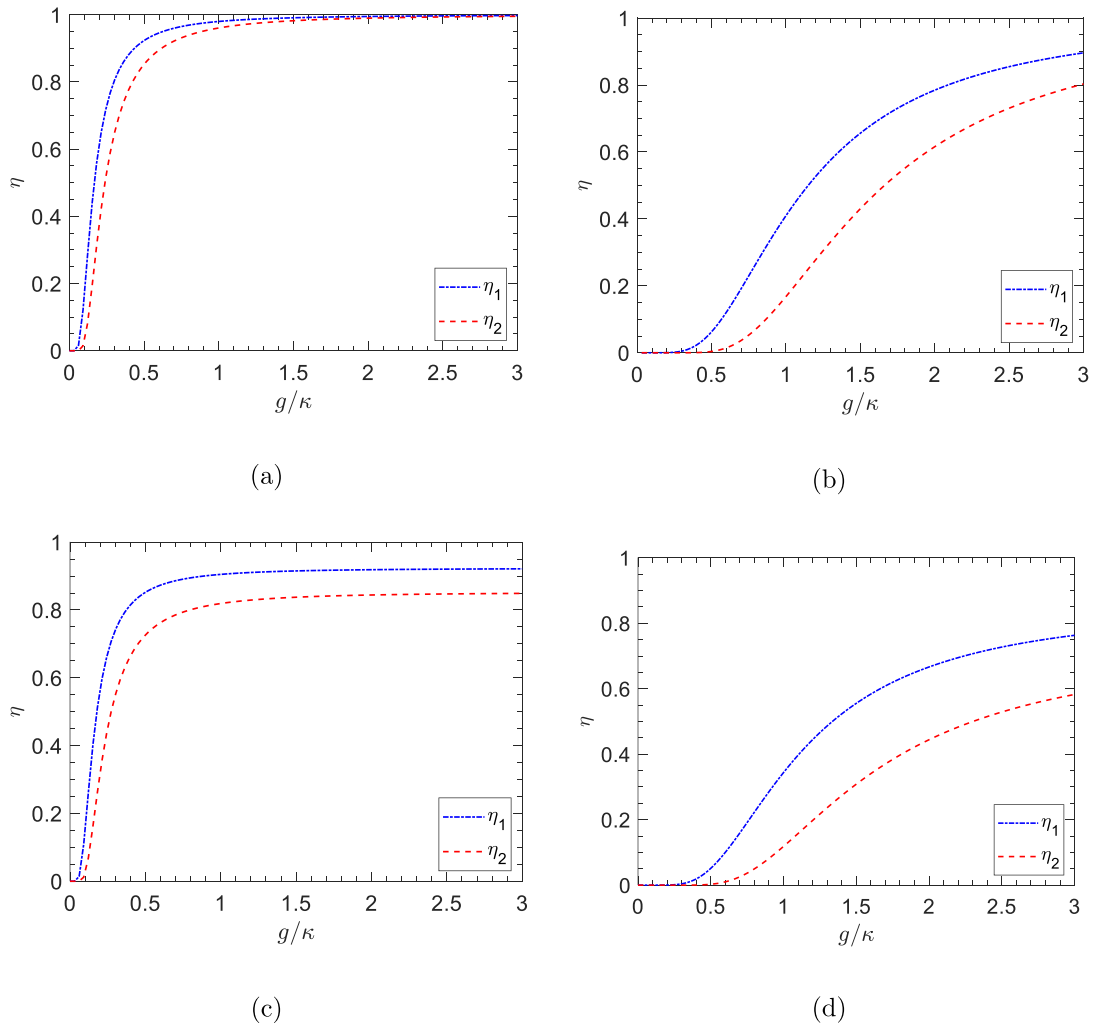

Figure 5. The relation between the efficiencies η_1 and η_2 and the coupling rate g/κ for the following conditions: (a) $\Delta = 0$ and $\kappa_s/\kappa = 0$; (b) $\Delta = \pm g$ and $\kappa_s/\kappa = 0$; (c) $\Delta = 0$ and $\kappa_s/\kappa = 0.01$; (d) $\Delta = \pm g$ and $\kappa_s/\kappa = 0.01$. Here, we take $\gamma = 0.01\kappa$.

η_1 and η_2 from 88.60% and 78.49% to 92.02% and 84.68%, respectively. It is evident that under the frequency detuning condition $\Delta = \pm g$, the efficiencies of the two gates are reduced compared to those under the resonance condition $\Delta = 0$, yet they remain operational in figures 5(b) and (d). Overall, in addition to achieving a fidelity of one, our protocol also demonstrates high efficiency, laying a foundation for advancements in the field of high-dimensional quantum computing.

Our proposed method is not limited to NV centers but possesses broad applicability to other physical platforms with analogous level structures, such as ion traps, superconducting qubits, atoms, and quantum dots. In our demonstration, a composite system comprising two two-level systems (i.e. two ground states of two NV centers, yielding a total of $2 \times 2 = 4$ Hilbert space) possesses a four-dimensional Hilbert space identical to that of a native four-level qudit, signifying an identical theoretical capacity for information storage and processing. Evidently, the utilization of native qudits offers more advantages, such as more compact information encoding, potentially diminishing the requisite number of quantum information carriers. However, in certain physical implementations, the precise control of multiple low-dimensional systems can be more established and tractable than the direct fabrication and manipulation of a high-dimensional native qudit possessing an equivalent number of levels. For instance, the control methodologies for the NV centers, utilized as qubits, are already comparatively advanced. Consequently, our proposed protocols, within the context of current technological capabilities, may provide a more experimentally practical route towards the realization of high-dimensional quantum logic gates. The physical realization and precise control of quantum systems endowed with multiple stable energy levels typically present greater challenges compared to the implementation and control of two-level qubits, and multi-level systems often exhibit heightened sensitivity to environmental noise and decoherence, thereby posing significant impediments to their practical implementation. Thus, employing mature qubit technologies to

synthesize qudits could offer a more pragmatic approach for investigating the distinctive features of qudit-based computation in the near term.

If a native four-level system is utilized as the target qudit, the four levels naturally exist within a single quantum entity, obviating the need to construct coupling between two qubits. The complexity thus shifts from controlling the interaction between two qubits to directly controlling a single multi-level system. For certain specific qudit operations, a native four-level system might allow for the direct driving of desired transitions using single or fewer control pulses. For example, a meticulously designed microwave or laser pulse can directly induce a transition between energy levels $|1\rangle$ and $|3\rangle$ without needing to pass through intermediate levels or a combination of multiple qubit operations. This could potentially lead to a higher efficiency of high-dimensional gate operation. However, in native four-level systems, the spacing between energy levels may also be non-uniform, with some levels potentially being closer to each other. Precisely driving a specific transition without affecting other nearby transitions necessitates control fields of very high precision. Moreover, as energy levels are typically anharmonic, the transition frequencies for $|0\rangle \rightarrow |1\rangle, |1\rangle \rightarrow |2\rangle$, and $|2\rangle \rightarrow |3\rangle$ are all distinct, exacerbating the challenge of constructing high-dimensional quantum gates. Moreover, higher energy levels are generally more susceptible to decoherence and relaxation than the ground and first excited states. In native four-level systems, if higher excited states are utilized, the lifetimes of these states may be shorter, thereby limiting gate fidelity. In summary, if a native four-level system with an ideal energy level structure and good coherence properties can be identified, and if high-precision selective control pulses can be realized, then gate implementation might become simpler and faster due to more direct transition pathways. Conversely, if non-ideal level spacing leads to significant crosstalk, or if higher energy levels suffer from severe decoherence, or if precise multi-frequency control is difficult to achieve, then the control complexity for a native four-level system could be substantial.

In summary, we have successfully constructed qudit-based 4×4-dimensional CNOT gate and $4 \times 4\times$ 4-dimensional Toffoli gate for the photon-NV^- center hybrid system, capitalizing on the state-selected reflection property of the NV^- center confined within a one-sided cavity. Compared to traditional 2-qubit CNOT and Toffoli gates, the target and control qudits of these high-dimensional gates are encoded in the electron-spin states of NV^- centers and the polarization-spatial states of single photon, respectively. The encoding leads to lower resource overhead and decoherence, and shorter operation times, enabling storage and ultrafast QIT without auxiliary entangled states or additional qudits. Furthermore, the high-dimensional CNOT and Toffoli gates provide increased experimental flexibility, enhancing efficiency and fidelity under current technological capabilities and boosting the practical speed of quantum computing. The proposed protocol significantly impacts the effectiveness of QIT and establishes a clear pathway for advancing high-dimensional quantum computing, offering enhanced processing capabilities and superior performance.

Data availability statement

The data cannot be made publicly available upon publication because they contain sensitive personal information. The data that support the findings of this study are available upon reasonable request from the authors.

Acknowledgments

This work was supported in part by the Natural Science Foundation of China under Contract 61901420; in part by Fundamental Research Program of Shanxi Province under Contract 20230302121116.

Conflict of interest

The authors declare that there are no conflicts of interest related to this article.

References

[1] Gyongyosi L and Imre S 2019 *Comput. Sci. Rev.* **31** 51–71
[2] Yang F, Zhao D F, Wei C, Chen X Y, Wei S J, Wang H F, Long G L and Xin T 2024 *New J. Phys.* **26** 043011
[3] Chen X Y *et al* 2024 *New J. Phys.* **26** 033023
[4] Romero J, Giovannini D, Tasca D S, Barnett S M and Padgett M J 2013 *New J. Phys.* **15** 083047
[5] Ballance C J, Harty T P, Linke N M, Sepiol M A and Lucas D M 2016 *Phys. Rev. Lett.* **117** 060504
[6] Zhou Y R, Zhang Q F, Liu F F, Han Y H, Gao Y P, Fan L, Zhang R and Cao C 2024 *Opt. Express* **32** 2786–803
[7] Du F F, Fan G and Ren X M 2024 *Quantum* **8** 1342
[8] Barenco A, Bennett C H, Cleve R, DiVincenzo D P, Margolus N, Shor P, Sleator T, Smolin J A and Weinfurter H 1995 *Phys. Rev. A* **52** 3457–67
[9] Ma M, Tan Q L and Du F F 2025 *Opt. Express* **33** 23678–91

[10] Zhang J F, Burgarth D, Laflamme R and Suter D 2015 *Phys. Rev. A* **91** 012330
[11] Du F F and Ren X M 2025 *Opt. Laser Technol.* **180** 111440
[12] Mirhosseini M, Magaña-Loaiza O S, O'Sullivan M N, Rodenburg B, Malik M, Lavery M P J, Padgett M J, Gauthier D J and Boyd R W 2015 *New J. Phys.* **17** 033033
[13] Wei H R, Liu W Q and Kwek L C 2020 *New J. Phys.* **22** 093051
[14] Luo M X and Wang X J 2014 *Sci. China Phys. Mech.* **57** 1712–7
[15] Wang Y C, Hu Z X, Sanders B C and Kais S 2020 *Front. Phys.* **8** 589504
[16] Ralph T C, Resch K J and Gilchrist A 2007 *Phys. Rev. A* **75** 022313
[17] Liu W Q and Wei H R 2020 *New J. Phys.* **22** 063026
[18] Liu W Q, Wei H R and Kwek L C 2020 *Phys. Rev. Appl.* **14** 054057
[19] Campbell E T 2014 *Phys. Rev. Lett.* **113** 230501
[20] Howard M and Campbell E 2017 *Phys. Rev. Lett.* **118** 090501
[21] Bechmann-Pasquinucci H and Tittel W 2000 *Phys. Rev. A* **61** 062308
[22] Dixon P B, Howland G A, Schneeloch J and Howell J C 2012 *Phys. Rev. Lett.* **108** 143603
[23] Cerf N J, Bourennane M, Karlsson A and Gisin N 2002 *Phys. Rev. Lett.* **88** 127902
[24] Zhang L J, Silberhorn C and Walmsley I A 2008 *Phys. Rev. Lett.* **100** 110504
[25] Wang F M *et al* 2020 *Phys. Rev. A* **101** 032340
[26] Collins D, Gisin N, Linden N, Massar S and Popescu S 2002 *Phys. Rev. Lett.* **88** 040404
[27] Vértesi T, Pironio S and Brunner N 2010 *Phys. Rev. Lett.* **104** 060401
[28] Dada A C, Leach J, Buller G S, Padgett M J and Andersson E 2011 *Nat. Phys.* **7** 677–80
[29] Sheridan L and Scarani V 2010 *Phys. Rev. A* **82** 030301
[30] Liu Z and Fan H 2009 *Phys. Rev. A* **79** 064305
[31] Ecker S *et al* 2019 *Phys. Rev. X* **9** 041042
[32] Erhard M, Fickler R, Krenn M and Zeilinger A 2018 *Light-Sci. Appl.* **7** 17146–17146
[33] Ma M, Zhu Q and Du F F 2025 *Adv. Quantum Technol.*
[34] Du F F, Ma M, Bai Z Y and Tan Q l 2025 *Phys. Rev. A* **111** 2469–9926
[35] Cozzolino D, Da Lio B, Bacco D and Oxenløwe L K 2019 *Adv. Quantum Technol.* **2** 1900038
[36] Erhard M, Krenn M and Zeilinger A 2020 *Nat. Rev. Phys.* **2** 365–81
[37] Chi Y L, Yu Y, Gong Q H and Wang J W 2023 *Sci. China Inf. Sci.* **66** 180501
[38] Blok M S, Ramasesh V V, Schuster T, O'Brien K, Kreikebaum J M, Dahlen D, Morvan A, Yoshida B, Yao N Y and Siddiqi I 2021 *Phys. Rev. X* **11** 021010
[39] Cervera-Lierta A, Krenn M, Aspuru-Guzik A and Galda A 2022 *Phys. Rev. Appl.* **17** 024062
[40] Ringbauer M, Meth M, Postler L, Stricker R, Blatt R, Schindler P and Monz T 2022 *Nat. Phys.* **18** 1053–7
[41] Anderson B E, Sosa-Martinez H, Riofrío C A, Deutsch I H and Jessen P S 2015 *Phys. Rev. Lett.* **114** 240401
[42] Shor P W 1999 *SIAM Rev.* **41** 303–32
[43] Reed M D, DiCarlo L, Nigg S E, Sun L, Frunzio L, Girvin S M and Schoelkopf R J 2012 *Nature* **482** 382–5
[44] Yi X, Huo J, Liu G, Fan L, Zhang R and Cao C 2025 *EPJ Quantum Technol.* **12** 43
[45] Paetznick A and Reichardt B W 2013 *Phys. Rev. Lett.* **111** 090505
[46] Su W, Qin W, Miranowicz A, Li T and Nori F 2024 *Phys. Rev. A* **110** 052612
[47] Du F F, Fan G, Ren X M and Ma M 2023 *Adv. Quantum Technol.* **6** 2300201
[48] Wu Y M, Fan G and Du F F 2022 *Front. Phys.* **17** 51502
[49] Du F f, Ren X m, Fan G and Guo J 2025 *Opt. Lett.* **50** 1113–6
[50] Chen A M, Cho S Y and Kim M D 2012 *Phys. Rev. A* **85** 032326
[51] Zheng S B 2013 *Phys. Rev. A* **87** 042318
[52] Zahedinejad E, Ghosh J and Sanders B C 2015 *Phys. Rev. Lett.* **114** 200502
[53] Gullans M J and Petta J R 2019 *Phys. Rev. B* **100** 085419
[54] Yin H D, Li X X, Wang G C and Shao X Q 2020 *Opt. Express* **28** 35576–87
[55] Rasmussen S E, Groenland K, Gerritsma R, Schoutens K and Zinner N T 2020 *Phys. Rev. A* **101** 022308
[56] Su Q P, Zhang Y, Bin L and Yang C P 2022 *Front. Phys.* **17** 53505
[57] Baker A J, Huber G B P, Glaser N J, Roy F, Tsitsilin I, Filipp S and Hartmann M J 2022 *Appl. Phys. Lett.* **120** 054002
[58] Su Q P, Bin L, Zhang Y and Yang C P 2023 *Appl. Phys. Lett.* **122** 114001
[59] Zhang X Y, Cao C, Gao Y P, Fan L, Zhang R and Wang C 2023 *New J. Phys.* **25** 053039
[60] Lanyon B P, Barbieri M, Almeida M P, Jennewein T, Ralph T C, Resch K J, Pryde G J, O'Brien J L, Gilchrist A and White A G 2009 *Nat. Phys.* **5** 134–40
[61] Monz T, Kim K, Hänsel W, Riebe M, Villar A S, Schindler P, Chwalla M, Hennrich M and Blatt R 2009 *Phys. Rev. Lett.* **102** 040501
[62] Fedorov A, Steffen L, Baur M, da Silva M P and Wallraff A 2012 *Nature* **481** 170–2
[63] Gao C, Liu F F, Fan Z Q, Fan L, Zhang R and Cao C 2025 *IEEE J. Sel. Top.* **31** 1–12
[64] Takeda K, Noiri A, Nakajima T, Kobayashi T and Tarucha S 2022 *Nature* **608** 682–6
[65] Nie J H, Zi W and Sun X M (arXiv:2402.05053)
[66] Chow J M *et al* 2012 *Phys. Rev. Lett.* **109** 060501
[67] Xiu X M, Cui C, Geng X, Wang S L, Li Q Y, Dong H K, Dong L and Gao Y J 2018 *Opt. Commun.* **426** 308–12
[68] Ionicioiu R, Spiller T P and Munro W J 2009 *Phys. Rev. A* **80** 012312
[69] Li T, Gao J C, Deng F G and Long G L 2018 *Ann. Phys., NY* **391** 150–60
[70] Zi W, Li Q and Sun X M 2023 *2023 60th ACM/IEEE Design Automation Conf. (DAC)* pp 1–6
[71] Gao X Q, Erhard M, Zeilinger A and Krenn M 2020 *Phys. Rev. Lett.* **125** 050501
[72] Du F F, Ren X M and Guo J 2024 *Opt. Express* **32** 31633–43
[73] Liu T, Xu J, Zhang Y, Yu Y, Su Q P, Zhou Y H and Yang C P 2023 *Appl. Phys. Lett.* **123** 134002
[74] Du F F, Ren X M, Ma M and Fan G 2024 *Opt. Lett.* **49** 1229–32
[75] Liu F F, Gao C, Fan L, Yi X, Zhang R and Cao C 2025 *Opt. Express* **33** 11929–43
[76] Robledo L, Childress L, Bernien H, Hensen B, Alkemade P F A and Hanson R 2011 *Nature* **477** 574–8
[77] Du F F, Ma M and Tan Q l 2025 *Sci. Rep.* **15** 2505
[78] Xie Z, Liu Y, Mo X, Li T and Li Z 2021 *Phys. Rev. A* **104** 062409
[79] Shi F Z *et al* 2010 *Phys. Rev. Lett.* **105** 040504

[80] van der Sar T, Wang Z H, Blok M S, Bernien H, Taminiau T H, Toyli D M, Lidar D A, Awschalom D D, Hanson R and Dobrovitski V V 2012 *Nature* **484** 82–86
[81] Arroyo-Camejo S, Lazariev A, Hell S W and Balasubramanian G 2014 *Nat. Commun.* **5** 4870
[82] Hu C Y, Young A, O'Brien J L, Munro W J and Rarity J G 2008 *Phys. Rev. B* **78** 085307
[83] Zu C, Wang W B, He L, Zhang W G, Dai C Y, Wang F and Duan L M 2014 *Nature* **514** 72–75
[84] Togan E *et al* 2010 *Nature* **466** 730–4
[85] Du F-F, Ren X-M, Fan Z-G, Li L-H, Du X-S, Ma M, Fan G and Guo J 2024 *Opt. Express* **32** 1686–700
[86] Kosaka H and Niikura N 2015 *Phys. Rev. Lett.* **114** 053603
[87] Bernien H *et al* 2013 *Nature* **497** 86–90
[88] Wei H R and Long G L 2015 *Phys. Rev. A* **91** 032324
[89] Wang T J and Wang C 2014 *Phys. Rev. A* **90** 052310
[90] Gardiner C W and Collett M J 1985 *Phys. Rev. A* **31** 3761–74
[91] Siyushev P, Pinto H, Vörös M, Gali A, Jelezko F and Wrachtrup J 2013 *Phys. Rev. Lett.* **110** 167402
[92] Han Y H, Cao C, Fan L and Zhang R 2021 *Opt. Express* **29** 20045–62